Discrepancy in assimilated atmospheric CO over East Asia in 2015-2020 by assimilating satellite and surface CO measurements

Zhaojun Tang[1], Jiaqi Chen[1], Zhe Jiang[1]*

[1]School of Earth and Space Sciences, University of Science and Technology of China, Hefei, Anhui, 230026, China.

*Correspondence to: Zhe Jiang (zhejiang@ustc.edu.cn)

Abstract

Satellite and surface carbon monoxide (CO) observations have been widely used to investigate the sources and variabilities of atmospheric CO. However, comparative analyses to explore the effects of satellite and surface measurements on atmospheric CO assimilations are still lacking. Here we investigate the assimilated atmospheric CO over E. Asia in 2015-2020, via assimilating CO measurements from the Measurement of Pollution in the Troposphere (MOPITT) and China Ministry of Ecology and Environment (MEE) monitoring network. We find noticeable inconsistencies in the assimilations: the adjusted CO columns (Xco) are about 162, 173 and 172 ppb by assimilating surface CO measurements, in contrast to 138-144, 149-155 and 144-151 ppb by assimilating MOPITT CO observations over E. China, North China Plain (NCP) and Yangtze River Delta (YRD), respectively. These inconsistencies could be associated with possible representation errors due to differences between urban and regional CO backgrounds. Furthermore, the adjusted surface CO concentrations are about 631, 806 and 657 ppb by assimilating surface CO measurements, in contrast to 418-427, 627-639 and 500-509 ppb by assimilating MOPITT CO observations over E. China, NCP and YRD, respectively; assimilations of normalized surface CO measurements (to mitigate the influences of representation errors) indicate declines of CO columns (Xco) by about 2.2, 2.1, and 1.8 ppb/y, in contrast to 0.63-0.86, 0.97-1.29, and 1.0-1.27 ppb/y by assimilating MOPITT CO measurements over E. China, South Korea and Japan, respectively. These discrepancies reflect

the different vertical sensitivities of satellite and surface observations in the lower and free troposphere. This work demonstrates the importance to integrate information from satellite and surface measurements to provide a more accurate evaluation of atmospheric CO changes.

1. Introduction

Atmospheric CO is one of the most important pollutants and plays a key role in tropospheric chemistry. Sources of atmospheric CO include fossil fuel combustion, biomass burning, and oxidation of hydrocarbons. The importance of atmospheric CO has made it an essential target of global emission controls. Satellite measurements have been used to investigate atmospheric CO changes (Han et al., 2018; Hedelius et al., 2021; Gaubert et al., 2020). Inverse analyses based on satellite measurements further improved our understanding of CO sources. For example, Jiang et al. (2017) constrained global CO emissions in 2001-2015 by assimilating MOPITT CO observations. Zheng et al. (2018a) constrained E. Asian CO emissions in 2005-2016 using MOPITT CO observations. Müller et al. (2018) assimilated Infrared Atmospheric Sounding Interferometer (IASI) CO observations to assess the impacts of hydroxyl radical (OH) on derived CO emissions.

A major advantage of satellite measurements is the global covered observations. In addition, the pixel-based observations allow convenient comparison with grid-based model simulations. However, the limited vertical resolution implies that the retrieved lower tropospheric CO is affected by free tropospheric CO (Jiang et al., 2013; Buchholz et al., 2017; Hedelius et al., 2021), despite the joint retrieval of near-infrared (NIR) and thermal infrared (TIR) spectral data can enhance the sensitivity to lower tropospheric CO (Worden et al., 2010; Deeter et al., 2017). In contrast to lower tropospheric CO, free tropospheric CO is more susceptible to influences from factors such as long-range transport. Consequently, interpretation of satellite CO measurements requires disentangling the influences from local

and non-local sources.

Besides satellite observations, surface in-situ CO measurements have been used to analyze atmospheric CO variabilities (Bouarar et al., 2019; Kong et al., 2020; Squires et al., 2020). There are also recent advances to assess CO sources via assimilating surface CO measurements provided by air quality stations, particularly in China. For example, Peng et al. (2018) assimilated surface CO observations to optimize CO emissions in October 2014. Ma et al. (2019) assimilated surface CO observations to optimize CO emissions in September 2016. Feng et al. (2020) constrained CO emissions in December 2013 and 2017. In contrast to satellite measurements, surface CO observations have rapid responses to local CO emissions. Consequently, the interpretation of surface CO observations is less affected by non-local sources and sinks. However, the sparse distributions of surface stations dimmed the importance of surface CO observations. In addition, it is challenging to match in-situ surface measurements with grid-based model simulations because of noticeable representation errors (Schutgens et al., 2017) and possible uncertainties in the planetary boundary layer (PBL) mixing (Castellanos et al., 2011).

To sufficiently understand CO variabilities, people may take advantage of information from both satellite and surface measurements. For example, Chen et al. (2020) found decreasing trends of atmospheric CO concentrations from both MOPITT and surface CO measurements over YRD. However, comparative analyses to investigate the effects of satellite and surface CO measurements in data assimilation systems are still lacking, which poses a significant barrier to integrating the information provided by satellite and surface measurements in data assimilation applications. In this work, we investigate the assimilated atmospheric CO over E. Asia in 2015-2020, via assimilating CO measurements from the MOPITT and MEE surface observations, to explore the methodology of assimilating two types of measurements, as well as the impacts of CO emission declines in China on atmospheric CO

over E. Asia. This paper is organized as follows: In Section 2, we describe the CO observations, GEOS-Chem model, and Kalman Filter approach used in this work. In Section 3, we investigate the performances of satellite and surface measurements in Kalman Filter. Our conclusions follow in Section 4.

2. Data and Methodology

2.1 MOPITT CO measurements

The MOPITT instrument was launched on December 18, 1999 on the NASA/Terra spacecraft. The satellite is in a sun-synchronous polar orbit of 705 km and crosses the equator at 10:30 local time. The instrument makes measurements in a 612 km cross-track scan with a footprint of 22 km *x* 22 km and provides global coverage every three days. The MOPITT data used here were obtained from the joint retrieval (V8J) of CO from thermal infrared (TIR, 4.7μm) and near-infrared (NIR, 2.3μm) radiances using an optimal estimation approach (Worden et al., 2010; Deeter et al., 2017). The retrieved volume mixing ratios (VMR) are reported as layer averages of 10 pressure levels (surface, 900, 800, 700, 600, 500, 400, 300, 200, and 100 hPa). Following Jiang et al. (2017), we reject MOPITT data with CO column amounts less than $5x10^{17}$ molec/cm^2 and with low cloud observations. Since the NIR channel measures reflected solar radiation, only daytime data are considered. As shown in Fig. 1a, CO columns provided by MOPITT indicate decreasing trends over E. Asia in 2015-2020, consistent with reported CO variability (Zheng et al., 2018a; Chen et al., 2020; Hedelius et al., 2021). In addition, the vertical columns are converted to column-averaged dry-air mole fractions (Xco) in this work.

2.2 MEE surface CO measurements

We use MEE surface in-situ hourly CO concentration data (https://quotsoft.net/air/) for the period of 2015-2020. These real-time monitoring stations have the ability to report hourly

concentrations of critical pollutants from over 1670 sites in 2020, which have been widely used to investigate the sources and changes of atmospheric CO in China (Peng et al., 2018; Ma et al., 2019; Feng et al., 2020). Concentrations were reported by the MEE in units of mg/m^3 with a precision of $0.001mg/m^3$, under standard temperature (273 K) until 31 August 2018. This reference state was changed on 1 September 2018 to 298 K. We converted CO concentrations to ppb and rescaled post-August 2018 concentrations to standard temperature (273 K) to keep the consistency in the trend analysis. To ensure the reliability of the data before assimilation, we screened the data on the numerical range and time range. In the first step, we removed data with CO concentrations larger than 6000 ppb (~7.5 mg/m^3), and the selection of this empirical value is relatively close to the 7 mg/m^3 selected by Feng et al. (2020). In the second step, to ensure the rationality of the daily variation of the assimilation results, we eliminated 327 sites with missing data for more than 14 consecutive days, accounting for 19.5% of the total number of sites. Fig. 1b shows the trends of surface CO concentrations provided by MEE. There are high-density surface stations in E. China with significant decreasing trends of CO concentrations from 2015 to 2020.

2.3 GEOS-Chem model simulations

The GEOS-Chem chemical transport model (http://www.geos-chem.org, version 12-8-1) is driven by assimilated meteorological data of MERRA-2. Our analysis is conducted at a horizontal resolution of nested 0.5°x0.625° and employs the CO-only simulation in GEOS-Chem, which uses archived monthly OH fields from the full chemistry simulation (Fisher et al., 2017). The CO boundary conditions are updated every 3-hour from a global simulation with 4° × 5° resolution. Emissions in GEOS-Chem are computed by the Harvard-NASA Emission Component (HEMCO). Global default anthropogenic emissions are from the CEDS (Community Emissions Data System) (Hoesly et al., 2018). Regional emissions are replaced by MEIC (Multiresolution Emission Inventory for China) in China and MIX in other regions of Asia (Li et al., 2017). The total anthropogenic CO emissions in MEIC inventory are further scaled with linear projections based on Zheng et al. (2018b). Open fire emissions are from the

Quick Fire Emissions Dataset (QFED) (Darmenov and da Silva, 2015). The biogenic emissions of VOCs are calculated according to the Model of Emissions of Gases and Aerosols from Nature (MEGAN v2.1) (Guenther et al., 2006).

2.4 Kalman Filter approach

We employ the sub-optimal Kalman Filter (Todling and Cohn, 1994) to assimilate MOPITT and surface CO observations. As a brief description of the assimilation algorithm, the forward model (*M*) predicts CO concentration (x_{at}) at time *t*:

$$x_{at} = M_t x_{t-1} \qquad \text{(Eq. 1)}$$

The optimized CO concentrations can be expressed as:

$$x_t = x_{at} + G_t(y_t - K_t x_{at}) \qquad \text{(Eq. 2)}$$

where y_t is observation, K_t represents operation operator which projects CO concentrations from the model space to observation space. G_t is the Kalman Filter Gain matrix, which can be described as:

$$G_t = S_{at} K_t^T (K_t S_{at} K_t^T + S_\epsilon)^{-1} \qquad \text{(Eq. 3)}$$

where S_{at} and S_ϵ are model and observation covariance, respectively. The sub-optimal Kalman Filter has been applied in previous studies to provide quick optimization for initial and boundary atmospheric CO concentrations (Jiang et al., 2015; Jiang et al., 2017). Han et al. (2022) further provided a comparative analysis between sub-optimal Kalman Filter and a hybrid deep learning model to predict surface CO concentrations in China in 2015-2020, and found the good performance of Kalman Filter in respect to independent observations. We note that the optimization effect of sub-optimal Kalman Filter is expected to be weaker than more complicated methods such as Ensemble Kalman Filter, particularly because the latter can optimize CO emissions and concentrations simultaneously (Miyazaki et al., 2017; Feng et al., 2020), for example, Ma et al. (2019) indicated that updated anthropogenic emissions led to improved CO forecast by about 10% during the first 36 hour of forecasts.

The assimilations were started on July 1 2014 by assimilating MOPITT or MEE CO observations to produce optimized initial conditions on Jan 1 2015. The modeled CO concentrations are compared with observations and updated hourly, based on Eq. 2, and then forwarded to Eq. 1 for the model simulations in the next time step, i.e., the assimilation window is one hour. We assume fixed model errors (50%). The observation errors of satellite data are calculated based on the MOPITT error covariance matrix. The observation errors of surface observations include measurement errors and representative errors. The measurement errors are calculated following Feng et al. (2020): $\varepsilon_0 = ermax + 0.005 * \Pi_0$, where $ermax$ is the base error (6 ppb) and Π_0 represents the observed CO concentrations. The representation errors are calculated following Elbern et al. (2007) and Tang et al. (2013): $\varepsilon_r = \gamma\varepsilon_0\sqrt{\Delta l/L}$, where γ is a scaling factor (0.5), Δl is the model resolution (~56 km in this study), and L represents the range that observation can reflect, which depends on the station type (2 km for urban, 4 km for suburban). Given the measurement error ε_0 and the representative error ε_r, the total observation error is defined as $\varepsilon_t = \sqrt{\varepsilon_0^2 + \varepsilon_r^2}$. Furthermore, the "super-observation" method was applied in this work to further reduce the influence of representative error (Miyazaki et al., 2017; Feng et al., 2020):

$$\omega_j = 1/\varepsilon_j^2 \qquad \text{(Eq. 4)}$$

$$y_s = \sum_{j=1}^{k} \omega_j y_j / \sum_{j=1}^{k} \omega_j \qquad \text{(Eq. 5)}$$

$$1/\varepsilon_s^2 = \sum_{j=1}^{k} 1/\varepsilon_j^2 \qquad \text{(Eq. 6)}$$

where y_j is CO observation of the *j*th station, ω_j represents the weighting factor of the *j*th station, y_s and ε_s are the grid-based CO observations and errors (super-observation), respectively.

3. Results and Discussions

3.1 Kalman Filter assimilating MOPITT CO

We firstly assimilate MOPITT CO data with global simulations (4° × 5° resolution) to optimize E. Asian CO boundary conditions. Same to Jiang et al. (2017), the MOPITT profile and column data are assimilated individually to produce two types of CO boundary conditions. High resolution (0.5°x0.625°) Kalman Filter are performed within E. Asia domain via assimilating MOPITT profile and column data individually, and reading the corresponding CO boundary conditions. As shown in Fig. 2a, we find marked seasonality in surface CO concentrations: about 1200 ppb in winter and 600 ppb in summer over NCP in 2019. The assimilation of MOPITT CO has a small influence on CO concentrations at the surface level: the mean surface CO concentrations over E. China increased from 268 ppb to 289-296 ppb in 2015-2020 (Table 1). It could be associated with the limited sensitivity of MOPITT to lower tropospheric CO, as well as the revisit time of satellite measurements, i.e., MOPITT visits an individual model grid every 3 days. Thus, the adjustment of surface CO by Kalman Filter can be affected by biased CO emissions in the forward simulations with a 60-minute time step.

In contrast to CO at the surface level, the Kalman Filter led to marked enhancement of CO columns (Fig. 2b). As shown in Table 1, the modeled CO columns (Xco) over E. China in 2015-2020 were adjusted from about 101 to 121-127 ppb. The difference in the Kalman Filter by assimilating MOPITT column and profile data is small. Similarly, Fig. 3 exhibits the CO vertical profiles from model a priori simulations and Kalman Filter. Assimilations of different MOPITT CO data (blue lines) led to similar enhancement of CO abundances, except at high altitudes around 100 hPa. Furthermore, Fig. 4 demonstrates the relative differences between modeled and MOPITT CO columns in 2019. There are pronounced negative biases in the a priori simulations by about 40% (Fig. 4a). By contrast, the differences are dramatically mitigated by assimilating MOPITT CO column data (Fig. 4b). As shown in Table 2, the modeled CO columns (smoothed with MOPITT averaging kernels and sampled at MEE

209 locations) increased from 97 to 124-128 ppb over E. China in 2015-2020. The good agreement
210 between assimilations and MOPITT CO observations (129 ppb, Table 2) confirms the
211 efficiency of Kalman Filter assimilation in this work.

212 **3.2 Kalman Filter assimilating surface CO**

213 Fig. 2c (black line) shows MEE surface CO observations over NCP in 2019. The blue
214 line shows the model a priori surface CO concentrations, which are lower than observed CO
215 concentrations. The underestimated surface CO concentrations were reported in recent studies,
216 for example, Peng et al. (2018) found that modeled surface CO concentrations by WRF-Chem
217 (752 $\mu g/m^3$) are about 40% lower than MEE surface CO (1318 $\mu g/m^3$) in NCP in October 2014.
218 Bouarar et al. (2019) indicated an underestimation of surface CO concentrations in WRF-Chem
219 (about 1000 ppb) than surface observations (about 2000 ppb) in Beijing in January 2010. Feng
220 et al. (2020) demonstrated high MEE surface CO in December 2013, i.e., 2.18 mg/m^3 and 1.66
221 mg/m^3 in contrast to 0.86 mg/m^3 and 0.73 mg/m^3 in WRF/CMAQ simulations over NCP and
222 E. China, respectively.

223 We then assimilate MEE surface CO measurements to investigate the impacts of
224 assimilations on atmospheric CO. In contrast to Kalman Filter by assimilating MOPITT data,
225 the CO boundary conditions here are from a priori simulations. Fig. 2d (orange line) shows the
226 optimized surface CO concentrations in NCP in 2019. The assimilation of surface CO
227 measurements significantly improved the agreement between observations and model
228 simulations. As shown in Table 1, the modeled surface CO concentrations in 2015-2020
229 increased from 268 to 430 ppb over E. China, 445 to 630 ppb over NCP and 418 to 598 ppb
230 over YRD. The correlations between modeled and observed surface CO are enhanced from
231 0.707 to 0.934 over NCP in 2019. The enhancement of surface CO concentrations due to
232 assimilating surface CO measurements have been reported in recent studies. For example, Peng
233 et al. (2018) demonstrated enhancement of surface CO from 752 $\mu g/m^3$ to 1418 $\mu g/m^3$ in NCP

in October 2014. Feng et al. (2020) exhibited enhancement of surface CO from 0.73 mg/m^3 to 1.62 mg/m^3 in December 2013 over E. China. Furthermore, as shown in Table 2, the assimilation led to an increase in surface CO concentrations from 397 ppb to 631 ppb over E. China in 2015-2020, exhibiting better agreement with MEE observations (781 ppb).

3.3 Discrepancy in assimilated CO by assimilating satellite and surface data

As shown in Fig. 3, the modeled CO profile by assimilating MEE surface CO (red solid line) is higher than MOPITT-based CO concentrations (blue lines) in the lower troposphere. It indicates a possible discrepancy in the adjusted CO concentrations by assimilating satellite and surface observations. As shown in Table 2, the adjusted surface CO concentrations by assimilating MEE CO measurements are higher than those by assimilating MOPITT data in 2015-2020: 631 and 417-427 ppb over E. China; 806 and 627-639 ppb over NCP; 657 and 500-509 ppb over YRD. Similarly, the adjusted CO columns (Xco) by assimilating MEE CO measurements are higher than those by assimilating MOPITT data in 2015-2020 (Table 2): 162 and 138-144 ppb over E. China; 173 and 149-155 ppb over NCP; 172 and 144-151 ppb over YRD. On the other hand, the adjusted CO columns by assimilating MEE CO measurements are comparable with those by assimilating MOPITT data after the application of MOPITT averaging kernels (Table 2), which could be associated with the weaker sensitivity of MOPITT to lower free tropospheric CO.

MOPITT CO retrievals have been sufficiently evaluated. For example, Deeter et al. (2017) indicated that the bias in MOPITT CO column data was about 3% in respect to NOAA flask measurements. The higher CO columns by assimilating MEE CO measurements thus indicate possible overestimated enhancements on free tropospheric CO. Similarly, Feng et al. (2020) suggested a 186% enhancement of CO emissions over E. China via assimilating surface CO measurements. By contrast, the MOPITT-based CO emission estimates are comparable with a priori emissions in China (Elguindi et al., 2020). In addition, as shown in Fig. 4a, the

modeled CO columns from the boundary conditions are biased low by about 40%, which was not removed when assimilating MEE surface CO. While the influence from boundary conditions on surface CO concentrations over E. China could be limited, it is expected to have a noticeable influence on free tropospheric CO over E. China. It further confirms the overestimated enhancements on free tropospheric CO by assimilating MEE CO measurements, because potential negative biases due to the usage of a priori boundary conditions have been completely covered.

Fig. 1c-d exhibit the model a priori simulation and observed surface CO, as well as the ratios between observed and model a priori surface CO in 2019. The ratios are about 1.5 over high polluted areas such as NCP and 2-6 over low polluted areas (Fig. 1d). Because most MEE stations are urban air quality sites, the regional discrepancy in the ratios reveals possible influences from representation error, i.e., the regional CO backgrounds are lower than observations from urban stations, and the influences are stronger over low polluted areas. Despite representation errors have been considered in the covariance matrix in the Kalman Filter (Section 2.4), it seems that the mitigation of representation errors is limited. It is not surprising because the covariance matrix is supposed to contain random errors with Gaussian distribution, whereas representation errors due to differences between urban and regional backgrounds are systematic biases. In addition, insufficient parameterized processes such as PBL mixing can further contribute to the underestimation of modeled surface CO concentrations (Castellanos et al., 2011).

3.4 Kalman Filter assimilating normalized surface CO

The possible systematic biases imply it may not be a good idea to assimilate surface CO measurements to optimize free tropospheric CO directly. Alternatively, considering the good capability of models to capture the observed CO variabilities, we can scale surface CO measurements using the ratios between observations and models. The MEE surface CO

measurements will be scaled using the ratios shown in Fig. 1d in the following discussions. The actual effect of this adjustment is normalizing modeled and observed surface CO concentrations in 2019, and hence, Kalman Filter, by assimilating the normalized surface CO measurements can reflect the variabilities (i.e., trends) instead of magnitudes of CO concentrations. It should be noted that the ratios are expected to be affected by interannual variabilities of meteorological conditions as well as possible land usage changes. The land usage changes are supposed to be insignificant due to the limited studied period (i.e., 2015-2020). More efforts are needed in the future to evaluate the possible influence of meteorological condition changes on the inconsistency between observations and simulations.

Fig. 2e (orange line) shows surface CO concentrations in NCP in 2019 by assimilating normalized surface CO measurements. The magnitudes of model a priori (blue line) and Kalman Filter (orange line) are consistent in Fig. 2e due to the normalization of surface CO measurements. As shown in Table 2, the adjusted surface and column CO concentrations by assimilating normalized MEE CO measurements are closer to the a priori simulations in 2015-2020. The correlation between modeled and observed surface CO is 0.865 over NCP in 2019, which is lower than the correlation by assimilating raw surface CO measurements. Furthermore, we performed sensitivity assimilation to evaluate the effects of MOPITT pass time by only assimilating MEE CO measurements in the morning. As shown in Table 2, the assimilation of morning data led to lower surface and column CO concentrations, and thus, the discrepancy in the CO columns (Section 3.3) is not driven by different temporal resolutions between satellite and surface CO observations.

3.5 Assimilated atmospheric CO over E. Asia in 2015-2020

Here we expand our analysis to investigate the assimilated atmospheric CO over E. Asia in 2015-2020. As shown in Fig. 5a, Kalman Filter, by assimilating raw surface CO measurements reveal wide declines in surface CO concentrations over E. China. The declines

of surface CO resulted in decreases of CO columns (Fig. 5b, via assimilating normalized surface CO measurements) by about 2.2, 2.1 and 1.8 ppb/y in 2015-2020 over E. China, South Korea and Japan, respectively. By contrast, the decreasing trends in the MOPITT-based assimilations (Fig. 5c-d) are weaker: 0.63-0.86, 0.97-1.29 and 1.00-1.27 ppb/y in 2015-2020 over E. China, South Korea and Japan, respectively. It should be noted that the decreasing trends in the MOPITT-based assimilations are more affected by the a priori simulations and are thus, weaker than those of MOPITT observations, as exhibited by the neutral changes over central China in Fig. 5c-d. In addition, Fig. 5e demonstrates the trends of CO columns by assimilating both MOPITT CO column and normalized surface CO measurements simultaneously: the decreasing trends are about 2.3, 2.2 and 1.9 ppb/y over E. China, South Korea and Japan, respectively.

As shown in Fig. 6, the a priori simulations with fixed anthropogenic CO emissions in 2010 (black lines) predict stable surface CO concentrations in 2015-2020. By contrast, Kalman Filter by assimilating raw surface CO measurements (red solid lines) demonstrates declines in surface CO concentrations by about 43.9, 19.2 and 18.3 ppb/y over NCP, YRD and E. China, respectively. The difference between the a priori simulations (black lines) and assimilations (red solid lines) indicates the impacts of successful CO emission controls in China. In addition, Kalman Filter by assimilating normalized surface CO measurements (red dashed lines) indicates declines of surface CO concentrations by about 32.1, 14.4 and 10.3 ppb/y over NCP, YRD and E. China, respectively.

Finally, we analyze the interannual variabilities of CO columns by assimilating MOPITT and surface CO measurements. As shown in Fig. 7, Kalman Filter by assimilating normalized surface CO measurements (red dashed lines) demonstrates declines of CO columns by about 4.4, 2.8 and 2.2 ppb/y in 2015-2020 over NCP, YRD and E. China, respectively. Kalman Filter by assimilating raw surface CO measurements (red solid lines) led to overestimated CO

columns. Kalman Filter by assimilating MOPITT observations (blue lines) exhibits smaller changes in CO columns: 1.2-1.5, 0.76-0.9 and 0.63-0.86 ppb/y in 2015-2020 over NCP, YRD and E. China, respectively. Kalman Filter by assimilating both MOPITT CO column and normalized surface CO measurements simultaneously (purple lines) exhibits decreasing trends of CO columns by about 4.5, 2.8 and 2.3 ppb/y in 2015-2020 over NCP, YRD and E. China, respectively.

4. Conclusion

A comparative analysis is provided in this work to explore the effects of satellite and surface measurements on atmospheric CO assimilations over E. Asia in 2015-2020. We find possible inconsistencies by assimilating satellite and surface CO measurements: the adjusted CO columns (Xco) are about 161, 173 and 172 ppb by assimilating surface CO measurements, in contrast to 138-144, 149-155 and 144-151 ppb by assimilating MOPITT CO observations in 2015-2020 over E. China, NCP and YRD, respectively. This difference is larger than the reported uncertainties in MOPITT CO columns (Deeter et al., 2017) and similar to the reported discrepancy in the derived CO emissions based on MOPITT and surface CO measurements (Elguindi et al., 2020; Feng et al., 2020). In addition, we find large regional discrepancies in the ratios between observed and model a priori surface CO: about 1.5 over high polluted areas such as NCP and 2-6 over low polluted areas (Fig. 1d). These inconsistencies could be associated with possible representation errors due to differences between urban and regional CO backgrounds, which cannot be effectively contained via adjusting the covariance matrix in the assimilations.

Assimilations of raw surface CO measurements indicate declines in surface CO concentrations by about 43.9, 19.2 and 18.3 ppb/y over NCP, YRD and E. China in 2015-2020. Assimilations of normalized surface CO measurements further indicate declines of CO columns (Xco) by about 2.2, 2.1 and 1.8 ppb/y over E. China, South Korea and Japan in 2015-

2020, respectively. It demonstrates the important impacts of CO emission controls in China on E. Asian atmospheric CO changes. By contrast, assimilations of MOPITT CO measurements suggest small trends in CO columns: 0.63-0.86, 0.97-1.29 and 1.00-1.27 ppb/y over E. China, South Korea and Japan in 2015-2020, respectively. These discrepancies reflect the different vertical sensitivities of satellite and surface observations to CO concentrations in the lower and free troposphere. While the normalized CO measurements in this work are supposed to provide a better representation of atmospheric CO in the free troposphere, Kalman Filter by assimilating raw CO measurements is closer to real urban CO concentrations at the surface level. More efforts to analyze the effects of meteorological variabilities on observed and modeled surface CO concentrations are helpful for better assimilation of surface CO observations, and more accurate evaluation of atmospheric CO changes.

Data availability: The MEE CO data can be downloaded from https://quotsoft.net/air/. The MOPITT CO data can be downloaded from https://asdc.larc.nasa.gov/data/MOPITT/. The GEOS-Chem model (version 12.8.1) can be downloaded from http://wiki.seas.harvard.edu/geos-chem/index.php/GEOS-Chem_12#12.8.1.

Competing interests: The authors declare that they have no conflict of interest.

Acknowledgments: We thank the providers of the MOPITT CO data; We thank the China Ministry of Ecology and Environment (MEE) for providing the surface CO measurements. The numerical calculations in this paper have been done on the supercomputing system in the Supercomputing Center of University of Science and Technology of China. This work was supported by the Hundred Talents Program of Chinese Academy of Science and National Natural Science Foundation of China (41721002).

Figure Legends

Table 1. Averages and trends of surface (T 1.1) and column (T 1.2) CO concentrations in 2015-2020. The domain definitions are shown in Fig. 1a. The E. Asian CO boundary conditions are provided by global a priori simulations, except Kalman Filters by assimilating MOPITT CO while the boundary conditions are provided by global assimilations of MOPITT CO. The "MEE normalized and MOPITT column" is performed by assimilating both MOPITT CO and normalized surface CO measurements simultaneously.

Table 2. Averages, correlations and trends of surface (T 2.1) and column (T 2.2 and T 2.3) CO concentrations in 2015-2020, sampled at the locations of MEE stations. The domain definitions are shown in Fig. 1a. The correlations between simulations and MOPITT observations in T 2.3 are not shown because MOPITT averaging kernels are not applied.

Figure 1. (A) Trends of MOPITT CO columns (Xco) in 2015-2020 with unit ppb/y; (B) Trends of MEE surface CO concentrations in 2015-2020 with unit ppb/y; (C) Modeled (contour, a priori simulation) and observed (dotted) surface CO concentrations in 2019 with unit ppb; (D) Ratios between observed and modeled (a priori simulation) surface CO concentrations in 2019. The black boxes in panel A define the domains (land only) of E. China, NCP, YRD, South Korea and Japan. The areas outside of China are excluded in the E. China domain.

Figure 2. (A) surface CO concentrations over NCP in 2019 from a priori simulation and Kalman Filter by assimilating MOPITT CO; (B) same as panel a, but for CO columns; (C) surface CO concentrations from a priori simulation and MEE observations; (D) surface CO concentrations from a priori simulation, MEE observations and Kalman Filter by assimilating MEE CO; (E) surface CO concentrations from a priori simulation, MEE observations and Kalman Filter by assimilating normalized MEE CO.

Figure 3. CO profiles over NCP in 2019 from a priori simulations (black line), Kalman Filter by assimilating MOPITT CO (column: blue solid line; profile: blue dashed line) and MEE CO (raw data: red solid line; normalized data: red dashed line).

Figure 4. (A) relative difference between a priori simulation and MOPITT in 2019, calculated by (Model - MOPITT)/MOPITT; (B) same as panel A, but with Kalman Filter by assimilating MOPITT CO column data; (C) same as panel A, but with Kalman Filter by assimilating MOPITT CO profile data.

Figure 5. Trends of surface CO concentrations in 2015-2020 by assimilating (A) raw MEE CO and trends of CO columns in 2015-2020 by assimilating (B) normalized MEE CO, (C) MOPITT CO column data, (D) MOPITT CO profile data and (E) normalized MEE CO + MOPITT CO column data.

Figure 6. Surface CO concentrations in 2015-2020 from a priori simulations (black line), Kalman Filter by assimilating raw (red solid line) and normalized (red dashed line) MEE CO.

Figure 7. CO columns (Xco) in 2015-2020 from a priori simulations (black line), Kalman Filter by assimilating MOPITT CO columns (blue line), MEE CO (raw data: red solid line; normalized data: red dashed line) and MOPITT CO column + normalized MEE CO (purple line).

References

Bouarar, I., Brasseur, G., Petersen, K., Granier, C., Fan, Q., Wang, X., Wang, L., Ji, D., Liu, Z., Xie, Y., Gao, W., and Elguindi, N.: Influence of anthropogenic emission inventories on simulations of air quality in China during winter and summer 2010, Atmos Environ, 198, 236-256, 10.1016/j.atmosenv.2018.10.043, 2019.

Buchholz, R. R., Deeter, M. N., Worden, H. M., Gille, J., Edwards, D. P., Hannigan, J. W., Jones, N. B., Paton-Walsh, C., Griffith, D. W. T., Smale, D., Robinson, J., Strong, K., Conway, S., Sussmann, R., Hase, F., Blumenstock, T., Mahieu, E., and Langerock, B.: Validation of MOPITT carbon monoxide using ground-based Fourier transform infrared spectrometer data from NDACC, Atmos Meas Tech, 10, 1927-1956, 10.5194/amt-10-1927-2017, 2017.

Castellanos, P., Marufu, L. T., Doddridge, B. G., Taubman, B. F., Schwab, J. J., Hains, J. C., Ehrman, S. H., and Dickerson, R. R.: Ozone, oxides of nitrogen, and carbon monoxide during pollution events over the eastern United States: An evaluation of emissions and vertical mixing, Journal of Geophysical Research, 116, 10.1029/2010jd014540, 2011.

Chen, Y., Ma, Q., Lin, W., Xu, X., Yao, J., and Gao, W.: Measurement report: Long-term variations in carbon monoxide at a background station in China's Yangtze River Delta region, Atmos Chem Phys, 20, 15969-15982, 10.5194/acp-20-15969-2020, 2020.

The Quick Fire Emissions Dataset (QFED): Documentation of versions 2.1, 2.2 and 2.4, NASA Technical Report Series on Global Modeling and Data Assimilation NASA TM-2015-104606, Volume 38: http://gmao.gsfc.nasa.gov/pubs/docs/Darmenov796.pdf, 2015.

Deeter, M. N., Edwards, D. P., Francis, G. L., Gille, J. C., Martínez-Alonso, S., Worden, H. M., and Sweeney, C.: A climate-scale satellite record for carbon monoxide: the MOPITT Version 7 product, Atmos Meas Tech, 10, 2533-2555, 10.5194/amt-10-2533-2017, 2017.

Elbern, H., Strunk, A., Schmidt, H., and Talagrand, O.: Emission rate and chemical state estimation by 4-dimensional variational inversion, Atmos Chem Phys, 7, 3749-3769, 10.5194/acp-7-3749-2007, 2007.

Elguindi, N., Granier, C., Stavrakou, T., Darras, S., Bauwens, M., Cao, H., Chen, C., Denier van der Gon, H. A. C., Dubovik, O., Fu, T. M., Henze, D. K., Jiang, Z., Keita, S., Kuenen, J. J. P., Kurokawa, J., Liousse, C., Miyazaki, K., Müller, J. F., Qu, Z., Solmon, F., and Zheng, B.: Intercomparison of Magnitudes and Trends in Anthropogenic Surface Emissions From Bottom‐Up Inventories, Top‐Down Estimates, and Emission Scenarios, Earth's Future, 8, 10.1029/2020ef001520, 2020.

Feng, S., Jiang, F., Wu, Z., Wang, H., Ju, W., and Wang, H.: CO Emissions Inferred From Surface CO Observations Over China in December 2013 and 2017, J Geophys Res-Atmos, 125, 10.1029/2019jd031808, 2020.

Fisher, J. A., Murray, L. T., Jones, D. B. A., and Deutscher, N. M.: Improved method for linear carbon monoxide simulation and source attribution in atmospheric chemistry models illustrated using GEOS-Chem v9, Geosci Model Dev, 10, 4129-4144, 10.5194/gmd-10-4129-2017, 2017.

Gaubert, B., Emmons, L. K., Raeder, K., Tilmes, S., Miyazaki, K., Arellano, A. F., Jr., Elguindi, N., Granier, C., Tang, W., Barre, J., Worden, H. M., Buchholz, R. R., Edwards, D. P., Franke, P., Anderson, J. L., Saunois, M., Schroeder, J., Woo, J. H., Simpson, I. J., Blake, D. R., Meinardi, S., Wennberg, P. O., Crounse, J., Teng, A., Kim, M., Dickerson, R. R., He, H., Ren, X., Pusede, S. E., and Diskin, G. S.: Correcting model biases of CO in East Asia: impact on oxidant distributions during KORUS-AQ, Atmos Chem Phys, 20, 14617-14647, 10.5194/acp-20-14617-2020, 2020.

Guenther, A., Karl, T., Harley, P., Wiedinmyer, C., Palmer, P. I., and Geron, C.: Estimates of global terrestrial isoprene emissions using MEGAN (Model of Emissions of Gases and Aerosols from Nature), Atmos Chem Phys, 6, 3181-3210, 10.5194/acp-6-3181-2006, 2006.

Han, H., Liu, J., Yuan, H., Jiang, F., Zhu, Y., Wu, Y., Wang, T., and Zhuang, B.: Impacts of Synoptic Weather Patterns and their Persistency on Free Tropospheric Carbon Monoxide Concentrations and Outflow in Eastern China, J Geophys Res-Atmos, 123, 7024-7046, 10.1029/2017jd028172, 2018.

Han, W., He, T.-L., Tang, Z., Wang, M., Jones, D., and Jiang, Z.: A comparative analysis for a deep learning model (hyDL-CO v1.0) and Kalman Filter to predict CO concentrations in China, Geosci Model Dev, 10.5194/gmd-2021-420, 2022.

Hedelius, J. K., Toon, G. C., Buchholz, R. R., Iraci, L. T., Podolske, J. R., Roehl, C. M., Wennberg, P. O., Worden, H. M., and Wunch, D.: Regional and Urban Column CO Trends

and Anomalies as Observed by MOPITT Over 16 Years, J Geophys Res-Atmos, 126, 10.1029/2020jd033967, 2021.
Hoesly, R. M., Smith, S. J., Feng, L., Klimont, Z., Janssens-Maenhout, G., Pitkanen, T., Seibert, J. J., Vu, L., Andres, R. J., Bolt, R. M., Bond, T. C., Dawidowski, L., Kholod, N., Kurokawa, J.-i., Li, M., Liu, L., Lu, Z., Moura, M. C. P., O'Rourke, P. R., and Zhang, Q.: Historical (1750–2014) anthropogenic emissions of reactive gases and aerosols from the Community Emissions Data System (CEDS), Geosci Model Dev, 11, 369-408, 10.5194/gmd-11-369-2018, 2018.
Jiang, Z., Jones, D. B. A., Worden, H. M., Deeter, M. N., Henze, D. K., Worden, J., Bowman, K. W., Brenninkmeijer, C. A. M., and Schuck, T. J.: Impact of model errors in convective transport on CO source estimates inferred from MOPITT CO retrievals, J Geophys Res-Atmos, 118, 2073-2083, 10.1002/jgrd.50216, 2013.
Jiang, Z., Jones, D. B. A., Worden, J., Worden, H. M., Henze, D. K., and Wang, Y. X.: Regional data assimilation of multi-spectral MOPITT observations of CO over North America, Atmos Chem Phys, 15, 6801-6814, 10.5194/acp-15-6801-2015, 2015.
Jiang, Z., Worden, J. R., Worden, H., Deeter, M., Jones, D. B. A., Arellano, A. F., and Henze, D. K.: A 15-year record of CO emissions constrained by MOPITT CO observations, Atmos Chem Phys, 17, 4565-4583, 10.5194/acp-17-4565-2017, 2017.
Kong, L., Tang, X., Zhu, J., Wang, Z., Fu, J. S., Wang, X., Itahashi, S., Yamaji, K., Nagashima, T., Lee, H.-J., Kim, C.-H., Lin, C.-Y., Chen, L., Zhang, M., Tao, Z., Li, J., Kajino, M., Liao, H., Wang, Z., Sudo, K., Wang, Y., Pan, Y., Tang, G., Li, M., Wu, Q., Ge, B., and Carmichael, G. R.: Evaluation and uncertainty investigation of the NO_2, CO and NH_3 modeling over China under the framework of MICS-Asia III, Atmos Chem Phys, 20, 181-202, 10.5194/acp-20-181-2020, 2020.
Li, M., Zhang, Q., Kurokawa, J.-i., Woo, J.-H., He, K., Lu, Z., Ohara, T., Song, Y., Streets, D. G., Carmichael, G. R., Cheng, Y., Hong, C., Huo, H., Jiang, X., Kang, S., Liu, F., Su, H., and Zheng, B.: MIX: a mosaic Asian anthropogenic emission inventory under the international collaboration framework of the MICS-Asia and HTAP, Atmos Chem Phys, 17, 935-963, 10.5194/acp-17-935-2017, 2017.
Ma, C., Wang, T., Mizzi, A. P., Anderson, J. L., Zhuang, B., Xie, M., and Wu, R.: Multiconstituent Data Assimilation With WRF‐Chem/DART: Potential for Adjusting Anthropogenic Emissions and Improving Air Quality Forecasts Over Eastern China, J Geophys Res-Atmos, 10.1029/2019jd030421, 2019.
Miyazaki, K., Eskes, H., Sudo, K., Boersma, K. F., Bowman, K., and Kanaya, Y.: Decadal changes in global surface NO_x emissions from multi-constituent satellite data assimilation, Atmos Chem Phys, 17, 807-837, 10.5194/acp-17-807-2017, 2017.
Müller, J. F., Stavrakou, T., Bauwens, M., George, M., Hurtmans, D., Coheur, P. F., Clerbaux, C., and Sweeney, C.: Top‐Down CO Emissions Based On IASI Observations and Hemispheric Constraints on OH Levels, Geophys Res Lett, 45, 1621-1629, 10.1002/2017gl076697, 2018.

Peng, Z., Lei, L., Liu, Z., Sun, J., Ding, A., Ban, J., Chen, D., Kou, X., and Chu, K.: The impact of multi-species surface chemical observation assimilation on air quality forecasts in China, Atmos Chem Phys, 18, 17387-17404, 10.5194/acp-18-17387-2018, 2018.

Schutgens, N., Tsyro, S., Gryspeerdt, E., Goto, D., Weigum, N., Schulz, M., and Stier, P.: On the spatio-temporal representativeness of observations, Atmos Chem Phys, 17, 9761-9780, 10.5194/acp-17-9761-2017, 2017.

Squires, F. A., Nemitz, E., Langford, B., Wild, O., Drysdale, W. S., Acton, W. J. F., Fu, P., Grimmond, C. S. B., Hamilton, J. F., Hewitt, C. N., Hollaway, M., Kotthaus, S., Lee, J., Metzger, S., Pingintha-Durden, N., Shaw, M., Vaughan, A. R., Wang, X., Wu, R., Zhang, Q., and Zhang, Y.: Measurements of traffic-dominated pollutant emissions in a Chinese megacity, Atmos Chem Phys, 20, 8737-8761, 10.5194/acp-20-8737-2020, 2020.

Tang, X., Zhu, J., Wang, Z. F., Wang, M., Gbaguidi, A., Li, J., Shao, M., Tang, G. Q., and Ji, D. S.: Inversion of CO emissions over Beijing and its surrounding areas with ensemble Kalman filter, Atmos Environ, 81, 676-686, 10.1016/j.atmosenv.2013.08.051, 2013.

Todling, R., and Cohn, S. E.: Suboptimal schemes for atmospheric data assimilation based on the Kalman filter, Monthly Weather Review, 122, 10.1175/1520-0493(1994)122<2530:SSFADA>2.0.CO;2, 1994.

Worden, H. M., Deeter, M. N., Edwards, D. P., Gille, J. C., Drummond, J. R., and Nédélec, P.: Observations of near-surface carbon monoxide from space using MOPITT multispectral retrievals, Journal of Geophysical Research, 115, 10.1029/2010jd014242, 2010.

Zheng, B., Chevallier, F., Ciais, P., Yin, Y., Deeter, M. N., Worden, H. M., Wang, Y., Zhang, Q., and He, K.: Rapid decline in carbon monoxide emissions and export from East Asia between years 2005 and 2016, Environ Res Let, 13, 10.1088/1748-9326/aab2b3, 2018a.

Zheng, B., Tong, D., Li, M., Liu, F., Hong, C., Geng, G., Li, H., Li, X., Peng, L., Qi, J., Yan, L., Zhang, Y., Zhao, H., Zheng, Y., He, K., and Zhang, Q.: Trends in China's anthropogenic emissions since 2010 as the consequence of clean air actions, Atmos Chem Phys, 18, 14095-14111, 10.5194/acp-18-14095-2018, 2018b.

T1.1 Surface CO Concentrations (ppbv or ppbv/year)		E. China		NCP		YRD		South Korea		Japan	
		Mean	Trend	Mean	Trend	Mean	Trend	Mean	Trend	Mean	Trend
Observations	MOPITT profile surface layer	222.9	-0.95	338.3	-6.29	356.3	0.26	254.6	-1.58	168.1	-0.21
	MEE	781.4	-43.55	880.6	-79.85	700.1	-23.34	\	\	\	\
Model a priori	surface layer	267.8	-0.57	444.8	-2.60	417.6	-6.13	173.5	-1.78	150.5	-1.68
Kalman Filter by assimilating	MOPITT profile	295.8	-1.40	479.9	-4.11	446.6	-6.98	204.5	-2.59	175.5	-2.54
	MOPITT column	289.2	-0.74	469.2	-2.82	438.1	-6.23	195.5	-2.08	170.6	-1.96
	MEE raw	429.8	-18.31	630.1	-43.92	598.4	-19.17	236.3	-8.37	183.5	-5.51
	MEE normalized	283.7	-10.79	505.0	-32.47	418.0	-14.69	186.5	-5.30	157.2	-3.59
	MEE normalized (morning)	270.8	-6.67	462.8	-22.13	412.2	-10.02	177.5	-3.92	152.4	-2.80
	MEE normalized and MOPITT profile	290.6	-10.28	511.4	-32.10	421.1	-14.41	195.8	-4.37	166.0	-2.40
T1.2 CO Columns (Xco ppbv or ppbv/year)		E. China		NCP		YRD		South Korea		Japan	
		Mean	Trend	Mean	Trend	Mean	Trend	Mean	Trend	Mean	Trend
Observations	MOPITT Column	110.5	-0.86	128.4	-2.04	132.9	-0.84	115.9	-0.92	106.5	-0.71
Model a priori	Column	100.6	-0.53	114.0	-1.06	121.9	-0.59	92.5	-0.89	87.3	-0.94
Kalman Filter by assimilating	MOPITT profile	127.0	-0.63	141.7	-1.17	147.5	-0.76	117.6	-0.97	111.2	-1.00
	MOPITT column	120.9	-0.86	136.7	-1.46	141.1	-0.90	113.0	-1.29	106.6	-1.27
	MEE raw	131.9	-3.51	154.1	-6.73	167.9	-4.12	114.9	-3.13	104.2	-2.63
	MEE normalized	105.5	-2.21	125.4	-4.40	130.6	-2.80	97.1	-2.08	90.4	-1.83
	MEE normalized (morning)	101.7	-1.52	117.4	-3.24	123.9	-1.75	93.8	-1.56	88.1	-1.42
	MEE normalized and MOPITT column	113.0	-2.29	134.5	-4.49	137.5	-2.81	105.4	-2.16	98.0	-1.86

Table. 1. Averages and trends of surface (T 1.1) and column (T 1.2) CO concentrations in 2015-2020. The domain definitions are shown in Fig. 1a. The E. Asian CO boundary conditions are provided by global a priori simulations, except Kalman Filters by assimilating MOPITT CO while the boundary conditions are provided by global assimilations of MOPITT CO. The "MEE normalized and MOPITT column" is performed by assimilating both MOPITT CO and normalized surface CO measurements simultaneously.

T2.1 Surface CO sampled at MEE locations (ppbv or ppb/y)		E. China			NCP			YRD		
		Mean	R	Trend	Mean	R	Trend	Mean	R	Trend
CO observations	MEE CO	781.4	1.00	-43.55	880.6	1.00	-79.85	700.1	1.00	-23.34
Model a priori	surface CO	397.0	0.85	-1.07	602.7	0.69	-1.66	479.6	0.69	-7.43
Kalman Filter by assimilating	MOPITT CO profile (10 levels)	426.5	0.86	-2.12	639.0	0.69	-3.40	508.8	0.70	-8.25
	MOPITT CO column	417.9	0.85	-1.21	627.0	0.69	-1.88	500.1	0.69	-7.53
	MEE CO	631.2	0.98	-30.58	805.9	0.96	-62.24	656.7	0.95	-21.01
	MEE CO (normalized)	410.3	0.97	-18.61	677.9	0.96	-50.96	463.0	0.95	-18.23
	MEE normalized (morning)	398.4	0.90	-12.55	623.8	0.81	-32.77	469.2	0.76	-13.58
	MEE normalized and MOPITT profile	414.1	0.97	-18.24	681.7	0.96	-50.71	465.3	0.95	-18.01
T2.2 CO Columns Sampled at MEE locations and smoothed with MOPITT Aks (Xco ppbv or ppbv/year)		E. China			NCP			YRD		
		Mean	R	Trend	Mean	R	Trend	Mean	R	Trend
CO observations	Column CO of MOPITT	128.6	1.00	-1.14	136.6	1.00	-2.62	136.6	1.00	-1.22
Model a priori	Column CO	97.4	0.43	-0.20	95.2	0.40	-0.13	104.4	0.34	0.21
Kalman Filter by assimilating	MOPITT CO profile (10 levels)	128.2	0.55	-0.49	134.6	0.55	-1.60	134.8	0.42	0.17
	MOPITT CO column	124.1	0.56	-0.47	131.9	0.56	-1.55	131.1	0.44	0.26
	MEE CO	126.5	0.40	-2.98	128.8	0.55	-5.07	136.2	0.30	-1.54
	MEE CO (normalized)	105.3	0.42	-2.17	107.6	0.50	-3.18	113.1	0.33	-1.45
	MEE normalized (morning)	99.2	0.44	-1.14	98.6	0.43	-1.80	106.4	0.36	-0.28
	MEE normalized and MOPITT column	119.8	0.51	-1.48	131.2	0.57	-2.62	126.8	0.38	-0.80
T2.3 CO Columns Sampled at MEE locations (Xco ppbv or ppbv/year)		E. China			NCP			YRD		
		Mean	N/A	Trend	Mean	N/A	Trend	Mean	N/A	Trend
Model a priori	Column CO	117.7		-0.51	126.7		-1.08	125.1		-0.61
Kalman Filter by assimilating	MOPITT CO profile (10 levels)	143.9		-0.69	154.7		-1.26	150.6		-0.78
	MOPITT CO column	137.6		-0.83	149.3		-1.49	144.2		0.93
	MEE CO	161.6		-4.90	172.6		-8.11	172.2		-4.14
	MEE CO (normalized)	125.1		-3.07	141.0		-5.50	134.0		-2.90
	MEE normalized (morning)	119.5		-2.09	130.9		-3.98	127.1		-1.83
	MEE normalized and MOPITT column	136.4		-0.96	150.6		-2.14	147.2		0.10

Table. 2. Averages, correlations and trends of surface (T 2.1) and column (T 2.2 and T 2.3) CO concentrations in 2015-2020, sampled at the locations of MEE stations. The domain definitions are shown in Fig. 1a. The correlations between simulations and MOPITT observations in T 2.3 are not shown because MOPITT averaging kernels are not applied.

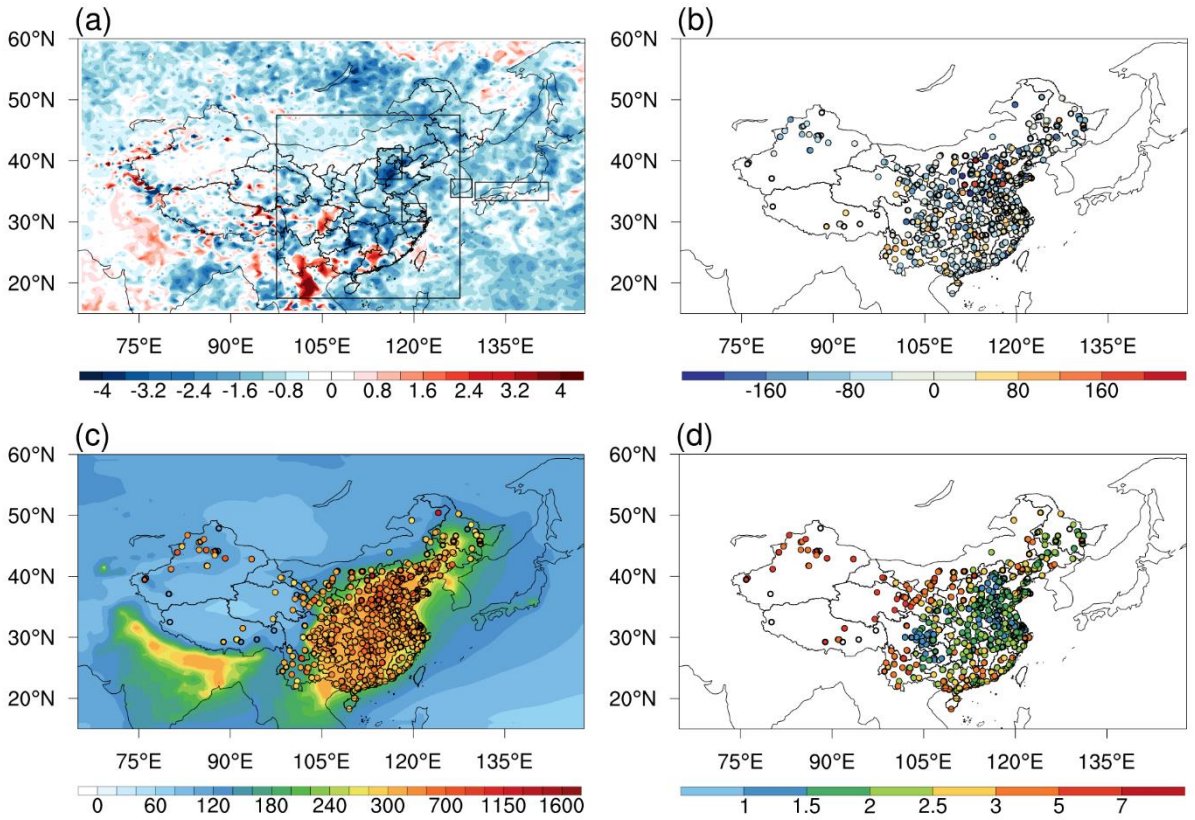

Fig. 1. (A) Trends of MOPITT CO columns (Xco) in 2015-2020 with unit ppb/y; (B) Trends of MEE surface CO concentrations in 2015-2020 with unit ppb/y; (C) Modeled (contour, a priori simulation) and observed (dotted) surface CO concentrations in 2019 with unit ppb; (D) Ratios between observed and modeled (a priori simulation) surface CO concentrations in 2019. The black boxes in panel A define the domains (land only) of E. China, NCP, YRD, South Korea and Japan. The areas outside of China are excluded in the E. China domain.

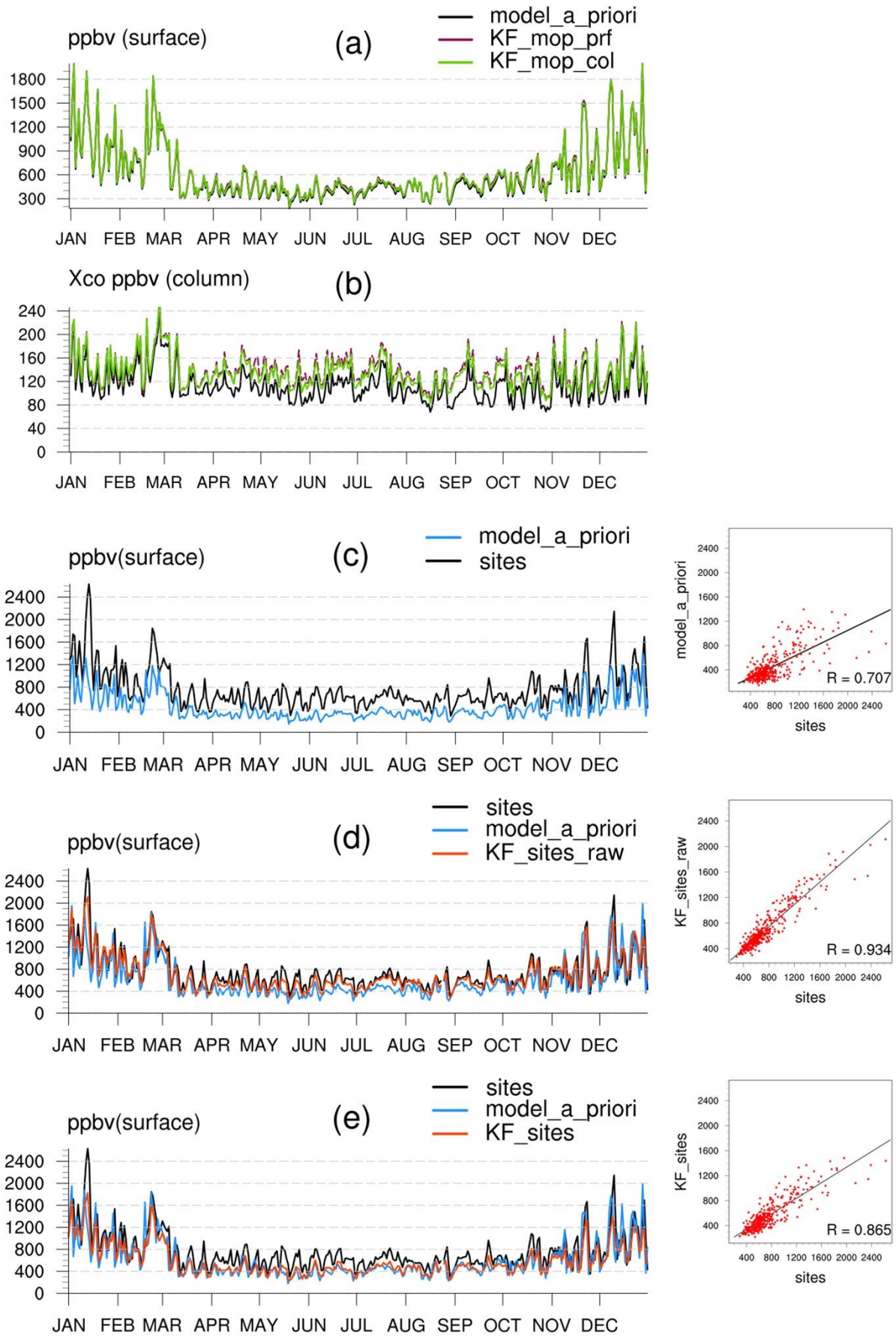
ppbv (surface)
(a)
model_a_priori
KF_mop_prf
KF_mop_col
1800
1500
1200
900
600
300
JAN FEB MAR APR MAY JUN JUL AUG SEP OCT NOV DEC
Xco ppbv (column)
(b)
240
200
160
120
80
40
0
JAN FEB MAR APR MAY JUN JUL AUG SEP OCT NOV DEC
ppbv(surface)
(c)
model_a_priori
sites
2400
2000
1600
1200
800
400
0
JAN FEB MAR APR MAY JUN JUL AUG SEP OCT NOV DEC
model_a_priori
R = 0.707
400 800 1200 1600 2000 2400
sites
ppbv(surface)
(d)
sites
model_a_priori
KF_sites_raw
JAN FEB MAR APR MAY JUN JUL AUG SEP OCT NOV DEC
KF_sites_raw
R = 0.934
sites
ppbv(surface)
(e)
sites
model_a_priori
KF_sites
JAN FEB MAR APR MAY JUN JUL AUG SEP OCT NOV DEC
KF_sites
R = 0.865
sites

Fig. 2. (A) surface CO concentrations over NCP in 2019 from a priori simulation and Kalman Filter by assimilating MOPITT CO; (B) same as panel a, but for CO columns; (C) surface CO concentrations from a priori simulation and MEE observations; (D) surface CO concentrations from a priori simulation, MEE observations and Kalman Filter by assimilating MEE CO; (E) surface CO concentrations from a priori simulation, MEE observations and Kalman Filter by assimilating normalized MEE CO.

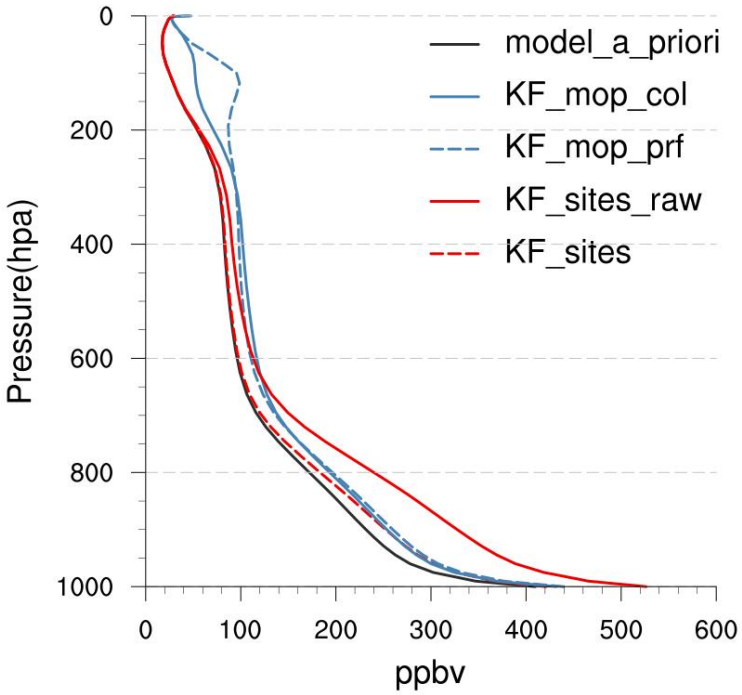

Fig. 3. CO profiles over NCP in 2019 from a priori simulations (black line), Kalman Filter by assimilating MOPITT CO (column: blue solid line; profile: blue dashed line) and MEE CO (raw data: red solid line; normalized data: red dashed line).

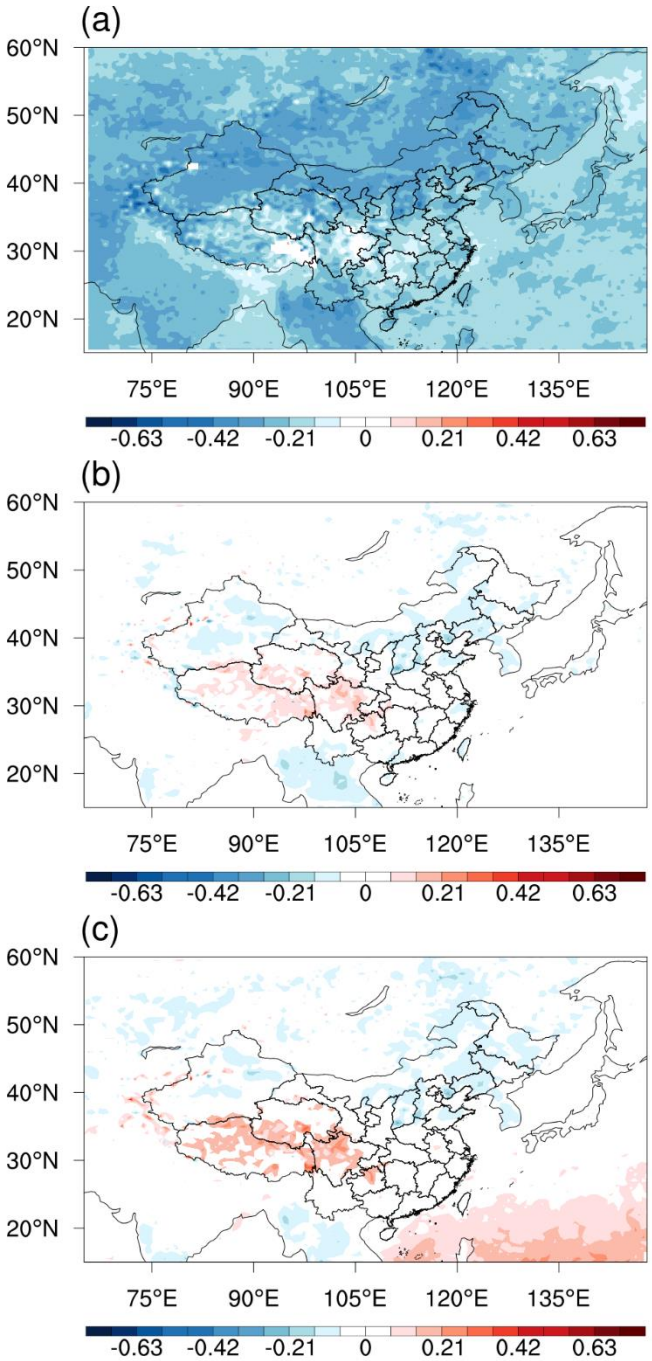

Fig. 4. (A) relative difference between a priori simulation and MOPITT in 2019, calculated by (Model - MOPITT)/MOPITT; (B) same as panel A, but with Kalman Filter by assimilating MOPITT CO column data; (C) same as panel A, but with Kalman Filter by assimilating MOPITT CO profile data.

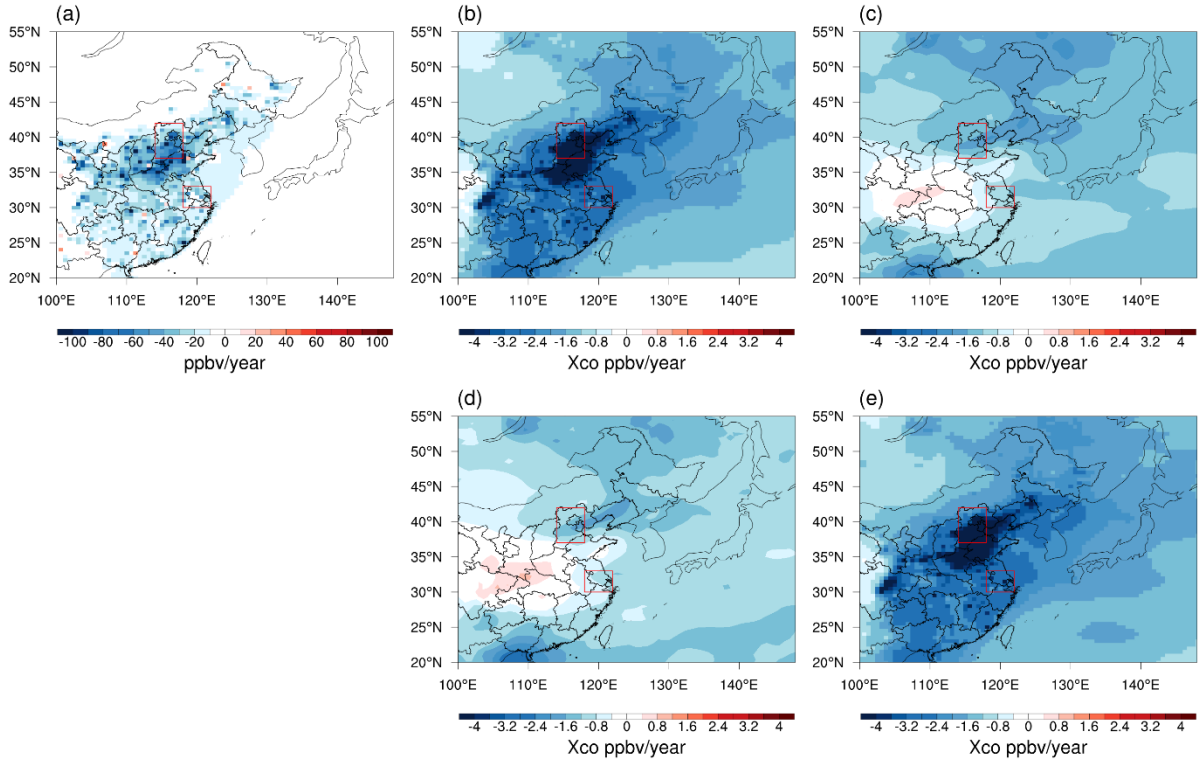

Fig. 5. Trends of surface CO concentrations in 2015-2020 by assimilating (A) raw MEE CO and trends of CO columns in 2015-2020 by assimilating (B) normalized MEE CO, (C) MOPITT CO column data, (D) MOPITT CO profile data and (E) normalized MEE CO + MOPITT CO column data.

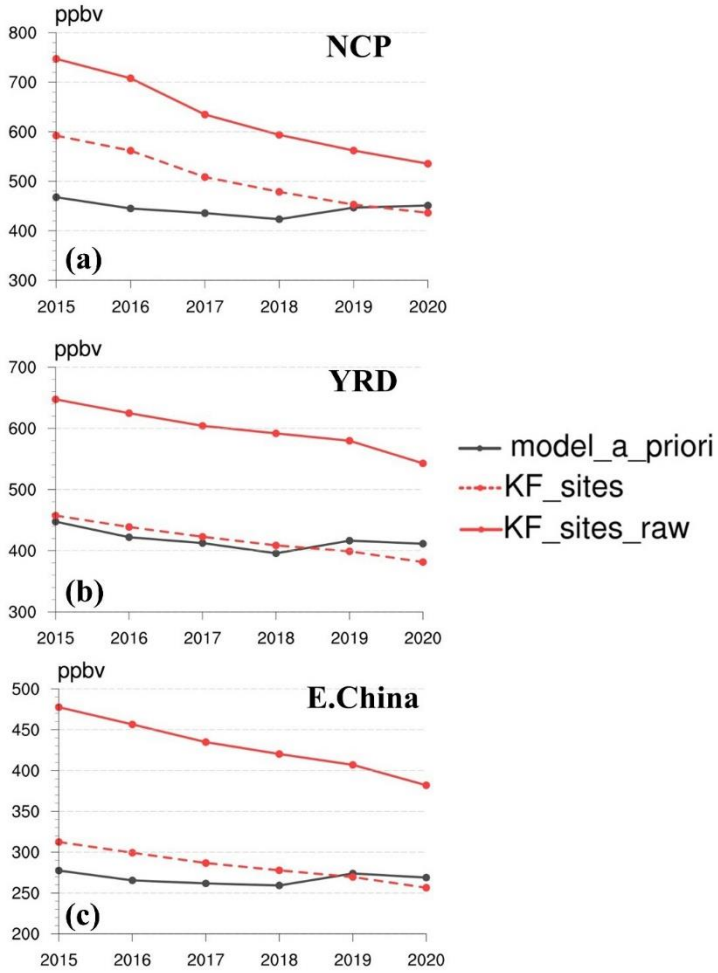

Fig. 6. Surface CO concentrations in 2015-2020 from a priori simulations (black line), Kalman Filter by assimilating raw (red solid line) and normalized (red dashed line) MEE CO.

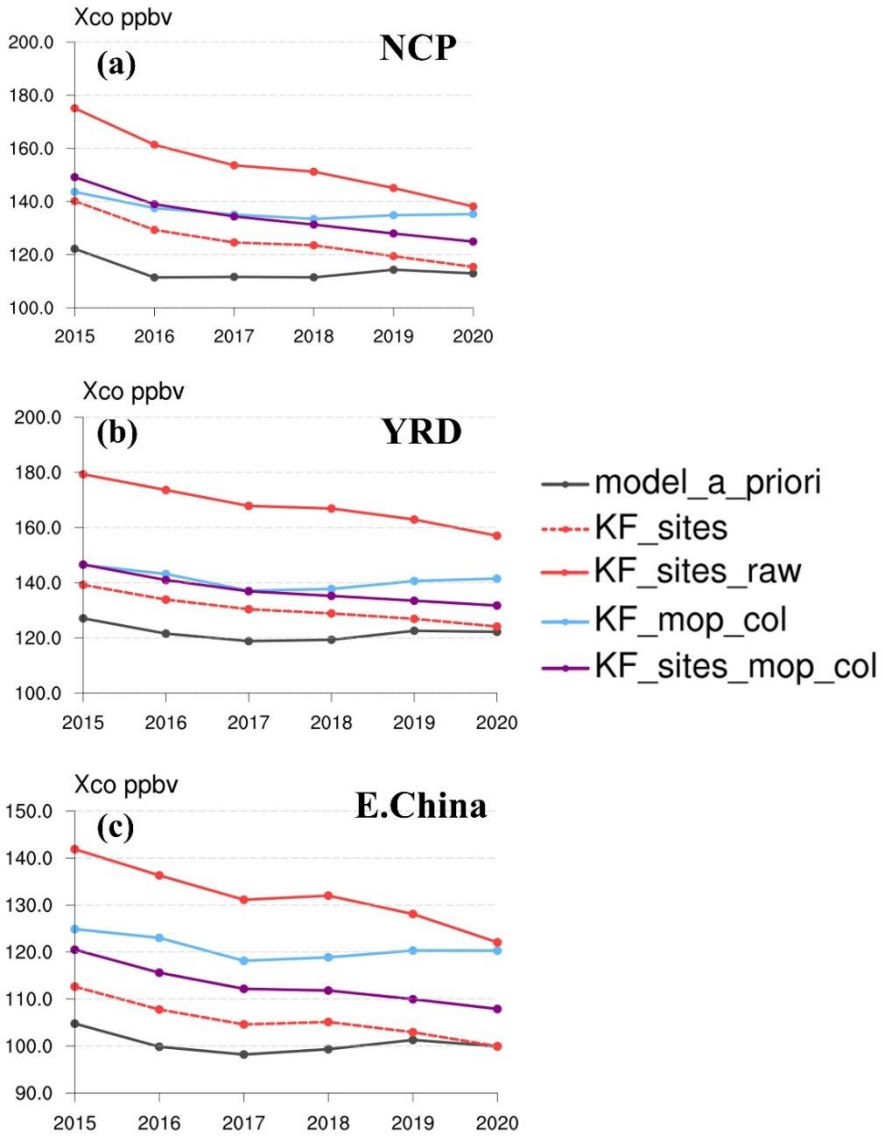

Fig. 7. CO columns (Xco) in 2015-2020 from a priori simulations (black line), Kalman Filter by assimilating MOPITT CO columns (blue line), MEE CO (raw data: red solid line; normalized data: red dashed line) and MOPITT CO column + normalized MEE CO (purple line).